

Molecular Beam Epitaxy of $\text{Al}_{1-x}\text{Sc}_x\text{N}$ Nanowires: Towards Group-III Nitride Piezoelectric Nanogenerators with Enhanced Response

Adriano Notarangelo,[†] Rudeesun Songmuang,[‡] Mostafa Saleh,[‡]
 Nattawadi Buatip,[‡] Ileana Florea,[¶] Philippe Vennéguès,[¶] Aidan F. Campbell,[†]
 Hans Tornatzky,[†] Jonas Lähnemann,[†] Thomas Auzelle,[†] Lutz Geelhaar,[†]
 Oliver Brandt,[†] and Philipp M. John^{*,†}

[†]*Paul-Drude-Institut für Festkörperelektronik, Leibniz-Institut im Forschungsverbund
 Berlin e.V., Hausvogteiplatz 5-7, 10117 Berlin, Germany*

[‡]*Université Grenoble Alpes, CNRS, Grenoble INP, Institut Néel, 38000 Grenoble, France*

[¶]*Université Côte d'Azur, CRHEA, CNRS, 06905 Sophia-Antipolis Cedex, France*

E-mail: john@pdi-berlin.de

Abstract

We study the molecular beam epitaxy of self-assembled $\text{Al}_{1-x}\text{Sc}_x\text{N}$ nanowires on conductive TiN layers and demonstrate their application in piezoelectric nanogenerators. Wurtzite $\text{Al}_{1-x}\text{Sc}_x\text{N}$ nanowires with uniform Sc incorporation are grown across a wide composition range ($0 < x < 0.35$). At substrate temperatures below 700 °C, these nanowires exhibit an inversely tapered morphology, whereas higher temperatures favor the nucleation of additional branches due to a phase separation of $\text{Al}_{1-x}\text{Sc}_x\text{N}$ into wurtzite AlN and rock-salt ScN. Phase-pure $\text{Al}_{1-x}\text{Sc}_x\text{N}$ nanowires are integrated into vertical nanogenerators, where the metallic TiN substrate serves as bottom electrode. The fabricated polymer–nanowire composite devices achieve effective piezoelectric charge coefficients of up to 8.5 pCN^{-1} at $x = 0.32$, thus exceeding the piezoelectric response of bulk AlN by nearly a factor of two. Although the charge response remains lower compared to $\text{Al}_{1-x}\text{Sc}_x\text{N}$ thin films, the reduced effective dielectric permittivity of the nanowire–polymer composites compensates

the reduction in piezoelectric charge coefficient, eventually yielding a higher voltage response and comparable energy harvesting efficiency. Finally, effective medium modeling reveals that the device architecture is the primary factor limiting performance, providing general design principles for highly efficient nanowire-based piezoelectric energy harvesters.

Keywords

ScAlN, nanowires, piezoelectric energy harvesting, phase separation, effective dielectric permittivity, transmission electron microscopy, AlScN, polarity

1 Introduction

Alloying hexagonal wurtzite group-III nitrides with cubic rock-salt transition metal nitrides has led to new ternary compounds with exciting properties.¹ The archetypal example is wurtzite $\text{Al}_{1-x}\text{Sc}_x\text{N}$, which exhibits

a piezoelectric charge coefficient up to five times higher than binary AlN for an optimum composition of $x \approx 0.35 - 0.40$.²⁻⁴ Moreover, ferroelectric switching of $\text{Al}_{1-x}\text{Sc}_x\text{N}$ thin films has been demonstrated in 2019,⁵ thus marking the first observation of ferroelectricity in a group-III nitride semiconductor. These new functionalities in $\text{Al}_{1-x}\text{Sc}_x\text{N}$ emerge from lattice frustrations caused by the substitution of tetrahedrally coordinated Al atoms by Sc, preferentially adopting an octahedral coordination.⁶ Although this mismatch renders wurtzite $\text{Al}_{1-x}\text{Sc}_x\text{N}$ metastable, it also opens new opportunities for device applications, including piezoelectric energy harvesting, which is currently dominated by lead-based compounds such as $\text{Pb}(\text{Zr},\text{Ti})\text{O}_3$ (PZT).

An attractive eco-friendly alternative to PZT-based piezoelectric devices are ZnO-based nanogenerators, first introduced in 2006.¹³ A key advantage of these devices is their mechanical flexibility that is given by the use of piezoelectric nanowires instead of bulk ceramics. Furthermore, the nanowire geometry enables high-quality growth on dissimilar substrates by elastic strain relaxation,¹⁴ thereby offering improvements in both performance and device integration. However, ZnO nanowires suffer from screening effects due to unintentional *n*-type doping, which limits their applicability for physiological sensing and energy harvesting at low frequencies. This doping typically arises from the inherent tendency of ZnO to incorporate native point defects (e.g., Zn interstitials and oxygen vacancies) or unintentional impurities such as hydrogen.¹⁵ One way to mitigate this issue is to replace ZnO by highly insulating AlN nanowires.¹⁶ However, their maximum theoretical performance is inferior to that of ZnO, as reflected by the respective bulk piezoelectric coefficients ($d_{33}^{\text{AlN}} \approx 5.4 \text{ pCN}^{-1}$ and $d_{33}^{\text{ZnO}} \approx 11.7 \text{ pCN}^{-1}$).^{17,18}

Here, we aim to employ $\text{Al}_{1-x}\text{Sc}_x\text{N}$ nanowires in vertically integrated piezoelectric nanogenerators (VINGs) in order to overcome the piezoelectric performance limit of AlN. To our knowledge, there are three reports on the synthesis of such nanowires

in the literature. Bohnen et al.¹⁹ pioneered the growth of $\text{Al}_{1-x}\text{Sc}_x\text{N}$ nanowires by hydride vapor phase epitaxy in 2009, but achieved only a very low Sc incorporation of $x = 0.05$. In contrast, Zhang et al.²⁰ sputtered $\text{Al}_{1-x}\text{Sc}_x\text{N}$ nanowires on TiN-buffered Si(111) substrates and achieved higher Sc contents ($0.08 < x < 0.17$), but with strong compositional gradients along the growth direction. Yet, their initial results point towards a strong enhancement of piezoelectric response upon Sc incorporation, similar to the thin film case. Finally, Wang et al.²¹ grew $\approx 100 \text{ nm}$ -long $\text{Al}_{1-x}\text{Sc}_x\text{N}$ segments on self-assembled GaN nanowires by plasma-assisted molecular beam epitaxy (MBE) and achieved a uniform Sc incorporation over a wide compositional range. However, the use of rather short $\text{Al}_{1-x}\text{Sc}_x\text{N}$ segments increases the probability of leakage currents, which would screen the piezoelectric charge during nanogenerator operation, particularly at low frequencies.

In this work, we grow $\approx 500 \text{ nm}$ long $\text{Al}_{1-x}\text{Sc}_x\text{N}$ nanowires on $\approx 200 \text{ nm}$ long AlN nanowire stems (referred to as $\text{Al}_{1-x}\text{Sc}_x\text{N}$ nanowires in the following), the latter self-assembled on 400 nm-thick TiN/Al₂O₃(0001) substrates as described in our previous works.²²⁻²⁴ We study growth over a wide temperature range, identify the optimum conditions to suppress phase separation, and achieve phase-pure wurtzite $\text{Al}_{1-x}\text{Sc}_x\text{N}$ nanowires over a large compositional range. Our self-assembly approach yields large-scale uniform nanowire ensembles and ensures simple device manufacturing by employing the metallic TiN substrate as an integrated bottom electrode. This allows us to demonstrate, for the first time, large-area proof-of-principle devices based on $\text{Al}_{1-x}\text{Sc}_x\text{N}$ nanowires, for which we evaluate the piezoelectric charge and voltage responses as well as the energy harvesting efficiency, and compare the results with bulk AlN and ZnO, and with commonly available $\text{Al}_{1-x}\text{Sc}_x\text{N}$ thin films.

2 Results and Discussion

2.1 Epitaxy, morphology and phase of $\text{Al}_{1-x}\text{Sc}_x\text{N}$ nanowires

We first study the impact of growth temperature during the plasma-assisted MBE of $\text{Al}_{1-x}\text{Sc}_x\text{N}$ nanowires on their morphology and crystalline phase. Figures 1a-c display representative cross-section secondary electron micrographs of $\text{Al}_{0.80}\text{Sc}_{0.20}\text{N}$ nanowires. Remarkably, decreasing the growth temperature from 1150 to 500 °C has drastic consequences for the ensemble morphologies. In particular, for $\text{Al}_{1-x}\text{Sc}_x\text{N}$ grown at the same temperature as the AlN stems (1150 °C, Figure 1a), long and thin nanowires form. Additionally, the high growth temperature induces extensive branching, with multiple branches nucleating and extending outward from the main body of each nanowire. In vapor-liquid-solid growth, this phenomenon usually occurs when catalyst droplets are intentionally deposited on the nanowire sidewalls, serving as new nucleation sites and giving rise to radial growth of branches.²⁵ For group-III nitride nanowires – grown in absence of any

catalyst – the self-induced branching observed here may result from phase separation of two structurally different materials, as similarly reported for $\text{In}_2\text{O}_3/\text{ZnO}$ nanowires.²⁶ Interestingly, a decrease of growth temperature to 830 °C first reduces the formation of branches (Figure 1b), until it is completely suppressed at 500 °C (Figure 1c). In contrast, these ensembles are characterized by an inversely tapered nanowire morphology. This shape is commonly attributed to a limited diffusion length of group-III adatoms impinging on the nanowire sidewall facets, thereby favoring radial over axial growth and, eventually, reducing the overall average nanowire elongation rate.^{24,27}

Next, we use Raman spectroscopy to determine the crystalline phase of our $\text{Al}_{1-x}\text{Sc}_x\text{N}$ nanowires. Figure 1d shows Raman spectra of ensembles grown in a wide temperature range, from 410 to 1150 °C. At low temperature, the spectra are characterized by a broad band at around 610 cm^{-1} , containing the contribution of several phonon modes. We attribute this series of peaks to phonon scattering in wurtzite $\text{Al}_{1-x}\text{Sc}_x\text{N}$. In particular, the three most intense contributions at 598,

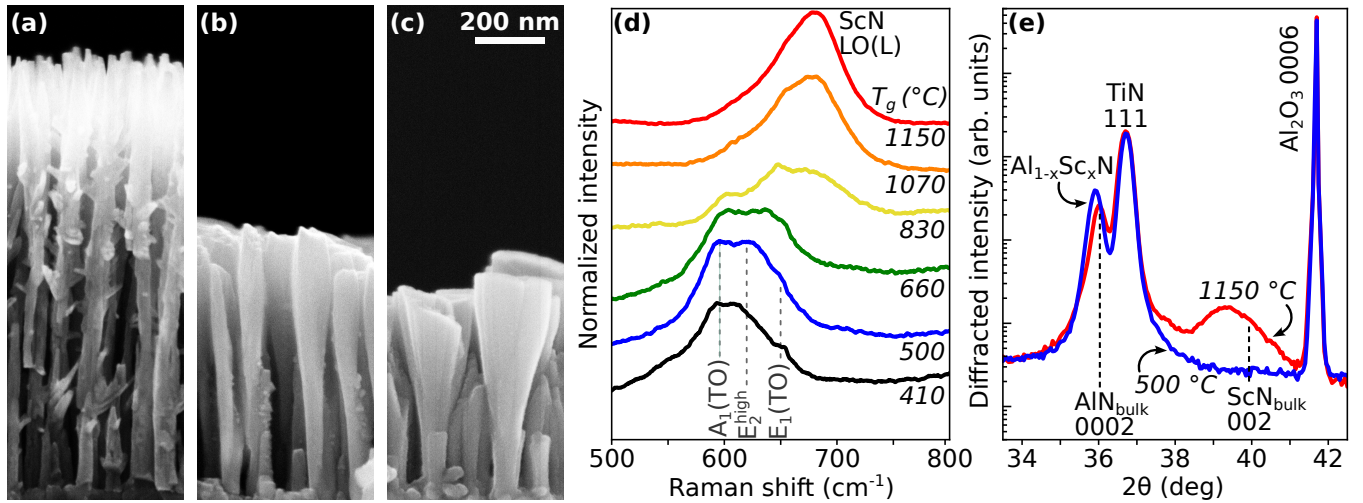


Figure 1: Cross-section secondary electron micrographs of $\text{Al}_{0.80}\text{Sc}_{0.20}\text{N}$ segments grown on self-assembled AlN nanowire stems at (a) 1150 °C, (b) 830 °C, and (c) 500 °C. (d) Room-temperature Raman spectra of several $\text{Al}_{0.80}\text{Sc}_{0.20}\text{N}$ nanowire ensembles grown at different temperatures (T_g), excited at 473 nm. Dashed lines indicate expected phonon positions of wurtzite $\text{Al}_{0.80}\text{Sc}_{0.20}\text{N}$,^{7,8} the peak at around 680 cm^{-1} is attributed to the LO(L) phonon of rock-salt ScN.^{9,10} (e) Symmetric XRD $2\theta/\omega$ scans of the nanowire ensembles shown in (a) and (c). Dashed lines show the expected peak positions for bulk AlN(0002) and ScN(002).^{11,12}

627 and 650 cm^{-1} in the ensemble grown at $500\text{ }^\circ\text{C}$ fit well to the $\text{A}_1(\text{TO})$, E_2^{high} , and $\text{E}_1(\text{TO})$ phonons reported for wurtzite $\text{Al}_{0.80}\text{Sc}_{0.20}\text{N}$, respectively.^{7,8} Increasing the growth temperature further leads first to a decrease of scattering intensity of these phonons ($660\text{ }^\circ\text{C}$), then to the appearance of a new band at around 680 cm^{-1} for growth temperatures $\geq 830\text{ }^\circ\text{C}$, eventually replacing the signal of wurtzite $\text{Al}_{1-x}\text{Sc}_x\text{N}$. This peak coincides with the LO(L) phonon of rock-salt ScN,^{9,10} thus supporting the hypothesis of branching being a result of phase separation into wurtzite AlN and rock-salt ScN. The formation of rock-salt ScN at high substrate temperatures can be attributed to an increased diffusivity of adatoms, allowing them to crystallize in their thermodynamically stable phases, namely wurtzite for AlN and rock-salt for ScN.

We use x-ray diffraction (XRD) to investigate the phase separation in our samples in more detail. Figure 1e compares symmetric $2\theta/\omega$ scans of the $\text{Al}_{0.80}\text{Sc}_{0.20}\text{N}$ nanowire ensembles grown at 500 and $1150\text{ }^\circ\text{C}$. Besides the peaks at 36.77° and 41.69° , corresponding to the TiN 111 and Al_2O_3 0006 reflections of the substrate, respectively, the diffractogram of the nanowires grown at $500\text{ }^\circ\text{C}$ exhibits one single peak at around 35.92° that we attribute to diffraction from $\text{Al}_{0.80}\text{Sc}_{0.20}\text{N}$ 0002 . The lower diffraction angle compared to bulk AlN 0002 ¹² evidences the incorporation of Sc that substitutes Al atoms in the wurtzite lattice. This substitution causes an increase in c -lattice constant as a function of Sc content for $0 \leq x \leq 0.2$, as observed in previous theoretical and experimental reports on $\text{Al}_{1-x}\text{Sc}_x\text{N}$ thin films.^{3,6} The nanowire ensemble grown at $1150\text{ }^\circ\text{C}$, on the other hand, exhibits two peaks apart from those of the substrate. The peak at 36.02° perfectly coincides with the position of bulk AlN 0002 and has a lower intensity than the $\text{Al}_{1-x}\text{Sc}_x\text{N}$ reflection of the ensemble grown at $500\text{ }^\circ\text{C}$. The broad peak at 39.48° is close to the position of bulk rock-salt ScN 002 ,¹¹ clearly evidencing a separation of $\text{Al}_{1-x}\text{Sc}_x\text{N}$ into wurtzite AlN and nanocrystalline rock-salt ScN at high growth temper-

atures. We attribute the deviation of the ScN 002 reflection towards lower angles compared to bulk ScN to the presence of strain at the AlN/ScN interface, resulting from the lattice mismatch between the two materials and/or a mismatch in their thermal expansion coefficients. Note that the incorporation of Al into the rock-salt ScN phase would lead to peak shifts towards higher angles and can thus be excluded.²⁸ Importantly, an epitaxial out-of-plane orientation-relationship between the wurtzite and rock-salt phases is found (cf. Figure 1e), where $\text{AlN}[0001] \parallel \text{ScN}[001]$. This orientation-relationship has been already observed between GaN and ScN during the growth of GaN/ScN core/shell nanowires,²⁹ as well as during the thermal decomposition of $\text{Al}_{1-x}\text{Sc}_x\text{N}$ thin films.³⁰ In both cases, the $[10\bar{1}0]$ direction of the respective group-III nitride aligns with the $[110]$ direction of ScN. By analogy, we propose that the full epitaxial orientation-relationship in our case is $\text{AlN}[0001](10\bar{1}0) \parallel \text{ScN}[001](110)$, consistent with the phase separation mechanisms observed in these previous works. The branches, growing at an angle of $(53 \pm 5)^\circ$ with respect to the nanowire axis, could then be the result of nucleation on the $\{111\}$ -facets of rock-salt ScN, where an angle of $\approx 55^\circ$ is expected.²⁹

2.2 Composition and microstructure of $\text{Al}_{1-x}\text{Sc}_x\text{N}$ nanowires

After identifying the appropriate growth parameter window to stabilize the wurtzite phase in $\text{Al}_{0.80}\text{Sc}_{0.20}\text{N}$ nanowires, we grow a sample series with varying Sc content x on 2 inch wafers. To this end, we vary the Sc flux, keeping the Al- and active N-fluxes constant. The growth temperature is kept below $700\text{ }^\circ\text{C}$, and is further decreased with increasing Sc content in order to avoid any phase separation (see Table 1 in Section 4.1 for more details). Figure 2a shows normalized energy dispersive x-ray spectroscopy (EDX) measurements of the different $\text{Al}_{1-x}\text{Sc}_x\text{N}$ nanowire ensembles recorded in a scanning electron microscope (SEM), which are used to deter-

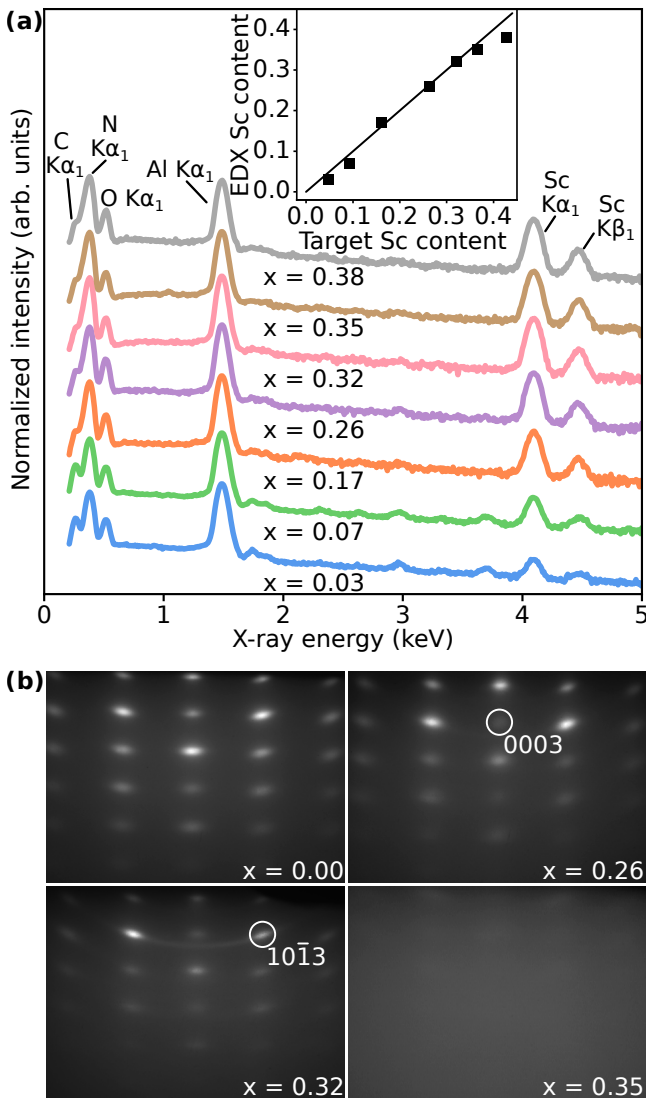


Figure 2: (a) Normalized SEM-EDX spectra of $\text{Al}_{1-x}\text{Sc}_x\text{N}$ nanowire ensembles with varying Sc content x , indicated below each spectrum. The inset shows the comparison with the target Sc content expected from the cell flux calibration. (b) RHEED patterns of selected ensembles (Sc content indicated in the bottom-right corner), recorded along the $[11\bar{2}0]$ azimuth. The AlN RHEED pattern was acquired after the growth of the nanowire stems. The RHEED patterns of $\text{Al}_{0.74}\text{Sc}_{0.26}\text{N}$ and $\text{Al}_{0.68}\text{Sc}_{0.32}\text{N}$ were recorded at the end of growth, whereas the pattern of $\text{Al}_{0.65}\text{Sc}_{0.35}\text{N}$ after half of its growth duration.

determine their composition. The ratio of the Sc-related peak intensities (K α_1 and Sc K β_1) to the Al K α_1 peak gradually increases progressively from the bottom to the top spectra, evidencing an increased Sc incorporation. After quantification with the eZAF routine (cf. Section 4.1), we obtain a Sc content between 0.03 and 0.38, covering essentially the entire accessible range for wurtzite $\text{Al}_{1-x}\text{Sc}_x\text{N}$.²⁻⁴ Moreover, the Sc content determined by EDX is in good agreement with the expected Sc content from the effusion cell flux calibration (see inset of Figure 2a).

To monitor the crystalline phase of the growing nanowires, we use reflection high-energy electron diffraction (RHEED). As displayed in Figure 2b, a transmission pattern is observed for the binary AlN nanowire stems, as expected for such group-III nitride nanostructures.^{24,31} The patterns of the $\text{Al}_{1-x}\text{Sc}_x\text{N}$ nanowires remain qualitatively unchanged until $x = 0.26$, indicating that the nanowires crystallize in the wurtzite structure. However, a decrease in diffracted intensity is observed for the wurtzite 0003 double diffraction spot, which has been associated with increased mosaicity in $\text{Al}_{1-x}\text{Sc}_x\text{N}$ thin films.³² In the case of our nanowire ensembles, this could be explained by an increased tilt angle between individual nanowires. Consistently, an increased intensity spread of the asymmetric Bragg reflections is found for the $\text{Al}_{0.68}\text{Sc}_{0.32}\text{N}$ nanowire ensemble, being most prominent for the 10̄13 peak. In addition, faint circular features appear in the pattern of this ensemble, evidencing the formation of a polycrystalline phase. As the Sc content increases further ($x = 0.35$), the RHEED pattern fades considerably, suggesting an amorphization that may occur as an intermediate phase towards the rock-salt phase of $\text{Al}_{1-x}\text{Sc}_x\text{N}$, typically emerging at $x \geq 0.35$.²⁸ Alternatively, the transition towards polycrystalline and amorphous phases for the nanowires with high Sc content may also be attributed to the well-known phenomenon of limited thickness epitaxy, occurring during the low-temperature MBE growth of various semiconductors.³³ This interpretation is consistent with the progressive decrease of crystalline quality observed by RHEED during the nanowire growth of ensembles with $x > 0.30$ (data not shown), noting that our $\text{Al}_{1-x}\text{Sc}_x\text{N}$

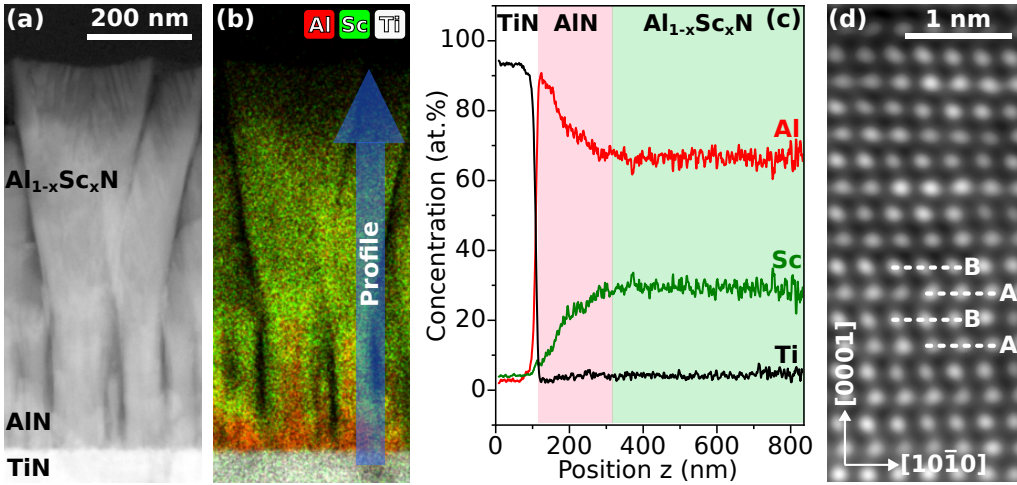


Figure 3: Structural and chemical investigation of $\text{Al}_{0.74}\text{Sc}_{0.26}\text{N}$ nanowires grown at 410°C by STEM. (a) HAADF image, (b) EDX map with (c) the corresponding EDX profile. (d) Fourier filtered high-resolution micrograph, evidencing wurtzite phase.

segments are thicker than most other MBE-grown $\text{Al}_{1-x}\text{Sc}_x\text{N}$ layers.

In order to investigate the microstructure and chemistry of our wurtzite nanowires, we analyze the $\text{Al}_{0.74}\text{Sc}_{0.26}\text{N}$ ensemble by scanning transmission electron microscopy (STEM). The overview high-angle annular dark field (HAADF) micrograph in Figure 3a reveals a morphology characterized by inverse nanowire tapering, consistent with the other low-temperature ensemble shown in Figure 1c. EDX mapping reveals a homogeneous incorporation of Sc into the $\text{Al}_{1-x}\text{Sc}_x\text{N}$ segment grown on AlN nanowire stems (Figure 3b). The extracted EDX profile (Figure 3c) confirms a composition of $x = 0.28$, in good agreement with the value found by the measurements in Figure 2a. Moreover, strong compositional fluctuations are absent along the nanowire axis and perpendicular to it on the investigated length scale. Finally, high-resolution imaging within the $\text{Al}_{1-x}\text{Sc}_x\text{N}$ segment clearly evidences an ABAB stacking sequence, characteristic for the desired wurtzite phase and in agreement with the RHEED analysis (Figure 2b).

2.3 $\text{Al}_{1-x}\text{Sc}_x\text{N}$ -based vertically integrated piezoelectric nanogenerators

To enable the use of our axial AlN/ $\text{Al}_{1-x}\text{Sc}_x\text{N}$ nanowires grown on TiN/ Al_2O_3 in functional piezoelectric devices, we process them into

vertically integrated nanogenerators (VINGs), as schematically illustrated in Figure 4a. First, a polymethyl methacrylate (PMMA) layer is spin-coated onto the nanowires to ensure high mechanical stability. Owing to the high degree of coalescence, the PMMA forms a smooth, approximately 60 nm-thick over-layer on top of the nanowires, with negligible penetration into the nanowire array. For the top contact we deposit Ni/Pt, while the metallic TiN layer serves as an integrated bottom contact. For each grown $\text{Al}_{1-x}\text{Sc}_x\text{N}$ ensemble, at least two large-area circular devices with a diameter of 0.8–1 mm are processed. The piezoelectric response of the VINGs is measured according to the Berlincourt method (i.e., in short-circuit conditions),³⁴ while electrical measurements in the same position are used to determine the device impedance.¹⁶ Further details on device fabrication and measurement are provided in the Section 4.1.

Figure 4b displays the charge signal of selected $\text{Al}_{1-x}\text{Sc}_x\text{N}$ piezoelectric nanogenerators with Sc contents of 0, 0.26, and 0.32 under a sinusoidal force excitation at 1 Hz. The stable operation at this frequency, indicating a high device impedance, evidences the absence of free carriers and underlines the suitability of such devices for piezoelectric energy harvesting at low frequencies typical for human body movements. Furthermore, a clear increase in amplitude is observed with increasing Sc content, reflecting enhanced piezoelectricity of the polymer-nanowire composite upon Sc incorporation.

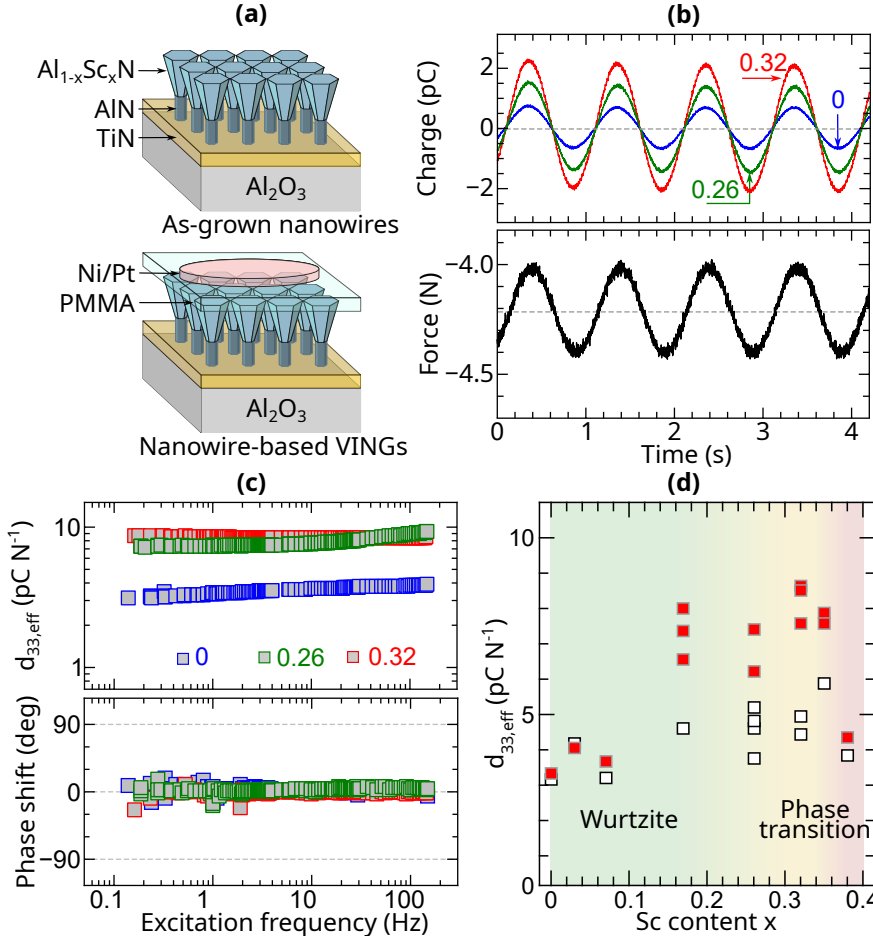


Figure 4: (a) Schematic illustration of $\text{Al}_{1-x}\text{Sc}_x\text{N}$ -based VINGs (bottom), processed from the MBE-grown $\text{Al}_{1-x}\text{Sc}_x\text{N}/\text{AlN}$ nanowires (top), the TiN layer serving as bottom contact. (b) Charge response of $\text{Al}_{1-x}\text{Sc}_x\text{N}$ VINGs with different Sc contents x to a sinusoidal force excitation at 1 Hz. (c) Extracted piezoelectric charge coefficient as a function of excitation frequency (upper panel), together with the phase shift between force and charge signals (lower panel). (d) $d_{33,\text{eff}}$ of all processed $\text{Al}_{1-x}\text{Sc}_x\text{N}$ VINGs as a function of Sc content x . The red data points highlight the devices with the strongest piezoelectric responses for each Sc content. The $\text{Al}_{1-x}\text{Sc}_x\text{N}$ VINGs outperform bulk AlN (d_{33} of 5.4 pCN^{-1}) in the composition range $0.15 \lesssim x \lesssim 0.35$.

Next, we extract the effective piezoelectric charge coefficient $d_{33,\text{eff}}$, corresponding to the ratio between the amplitude of the generated charge and that of the applied force, as well as the phase information from the device response. Figure 4c shows $d_{33,\text{eff}}$ as a function of excitation frequency in the range of 0.3–150 Hz. The piezoelectric output is almost constant in the entire frequency range, confirming the high mechanical and electrical stability of our nanogenerators. The phase shift, obtained by subtracting the phase of the force signal from that of the charge signal, remains zero for all samples in the measured frequency range. Based on our previous results,¹⁶ this indicates metal polarity of the $\text{Al}_{1-x}\text{Sc}_x\text{N}$ nanowires, consistent with the polarity of the AlN nanowire stems.^{16,22,35}

To evaluate the effect of Sc concentration on the performance of our $\text{Al}_{1-x}\text{Sc}_x\text{N}$ -based nanogenerators, Figure 4d shows $d_{33,\text{eff}}$ as a function of Sc content for all processed de-

vices, extracted at 1 Hz. Note that the devices with low Sc content already outperform the AlN-nanowire based devices of our previous work, which we attribute to differences in nanowire morphology and encapsulation method.¹⁶ In addition, a strong increase in $d_{33,\text{eff}}$ is observed for the best $\text{Al}_{1-x}\text{Sc}_x\text{N}$ nanowire-based devices (red data points) as a function of Sc content, with a maximum of 8.5 pCN^{-1} at $x = 0.32$. This value exceeds the piezoelectric coefficient of bulk AlN (5.4 pCN^{-1})¹⁷ by nearly a factor of two and approaches that of bulk ZnO (11.7 pCN^{-1}).¹⁸ The increase of the piezoelectric coefficient as a function of Sc content has been reported to result from a decrease in the c/a lattice parameter ratio of the ternary alloy, as well as to lattice softening induced by the incorporation of Sc into the wurtzite lattice.³⁶ For $x > 0.35$, $d_{33,\text{eff}}$ starts decreasing, most likely due to the onset of amorphization observed in high-Sc-content nanowire ensembles (cf. Fig-

ure 2b), which indicates the structural transition towards the non-piezoelectric rock-salt phase.²⁸ We attribute the strong scattering in our data to challenges in device processing and measurements, as well as to differences in nanowire length and composition between the center and edge of the 2 inch wafer. Yet, the overall trend of our VINGs evidences a strong increase of $d_{33,\text{eff}}$ upon Sc incorporation with an optimum (about $x \approx 0.32$), similar to the thin film case. However, the measured charge response remains well-below the values reported for $\text{Al}_{1-x}\text{Sc}_x\text{N}$ layers.

To interpret these results, we apply a theoretical effective-medium modeling approach and calculate the effective piezoelectric charge coefficient for the nanowire-composite devices as

$$d_{33,\text{eff}} = S_{33,\text{eff}} e_{33,\text{eff}} \quad (1)$$

where $S_{33,\text{eff}}$ and $e_{33,\text{eff}}$ are the effective elastic compliance and piezoelectric stress coefficient of the nanowire-polymer composite. To determine $S_{33,\text{eff}}$ and $e_{33,\text{eff}}$, our effective medium approach takes into account the effective elastic and piezoelectric properties of each individual component of our nanowire-polymer composite devices. The modeling is thus carried out in three consecutive steps:

(i) We calculate $S_{33,\text{eff}}$ and $e_{33,\text{eff}}$ of an $\text{Al}_{1-x}\text{Sc}_x\text{N}/\text{AlN}$ heterostructure under *iso-stress* conditions (i.e., identical internal pressure) along its [0001] direction, using the Sc-content-dependent elastic and piezoelectric properties of $\text{Al}_{1-x}\text{Sc}_x\text{N}$, and those of binary AlN reported in the literature.³ (ii) Using the results from (i), we calculate $S_{33,\text{eff}}$ and $e_{33,\text{eff}}$ of the active layer by forming a nanowire array, in which the nanowires are arranged in parallel and separated by air gaps. This configuration experiences *iso-strain* conditions (i.e., a common displacement) along the nanowire axis. (iii) Finally, we calculate the response of the full device by adding the PMMA encapsulation onto the active layer obtained from (ii) assuming *iso-stress* conditions, and calculate $d_{33,\text{eff}}$ using Equation (1). The exact formalism of our calculations is provided in Section 4.2.

Figure 5a displays again the experimentally obtained $d_{33,\text{eff}}$ as a function of Sc content, now overlayed with the results of our model. The calculations assume a heterostructure of 500 nm-long $\text{Al}_{1-x}\text{Sc}_x\text{N}$ segments on top of 200 nm-long AlN stems with a volume filling factor of 0.6, and a smooth, 60 nm-thick PMMA encapsulation layer. The model (black solid line) reproduces well the trend of our best devices. Note that we calculated the piezoelectric response of the $\text{Al}_{1-x}\text{Sc}_x\text{N}$ devices up to a Sc content of 0.5 assuming crystallization in the wurtzite phase. The reduction of $d_{33,\text{eff}}$ compared to $\text{Al}_{1-x}\text{Sc}_x\text{N}$ thin films is primarily attributed to the series coupling of the $\text{Al}_{1-x}\text{Sc}_x\text{N}$ segments with the less-piezoelectric AlN stems and the highly compliant, non-piezoelectric polymer. In contrast, the filling factor of the nanowire array has negligible influence on $d_{33,\text{eff}}$. This observation is highly promising and suggests that further improvements in device architecture – such as replacing AlN stems with conductive *n*-type GaN stems²¹ or eliminating them altogether through large-area top-down processing³⁶ – are expected to significantly enhance $d_{33,\text{eff}}$, potentially approaching the values reported for thin-film devices (dashed, grey line). Furthermore, the use of top-down fabrication strategies yielding improved nanowire morphology would allow the encapsulation polymer to penetrate into the nanowire array, enabling – beyond performance gains – a straightforward exfoliation for use in flexible devices.

Although $d_{33,\text{eff}}$ is essential to describe the piezoelectric properties of our nanowire-based devices, it should be noted that the electromechanical conversion efficiency of a given piezoelectric *voltage* coefficient $g_{33,\text{eff}} = d_{33,\text{eff}}/(\epsilon_0 \epsilon_{r,\text{eff}})$, where ϵ_0 is the vacuum permittivity and $\epsilon_{r,\text{eff}}$ is the effective relative static permittivity of the medium. To obtain this key figure of merit for sensing applications, we determine $\epsilon_{r,\text{eff}}$ from impedance measurements performed in the same position as the those used for the extraction of $d_{33,\text{eff}}$. In particular, the device capacitance is first ex-

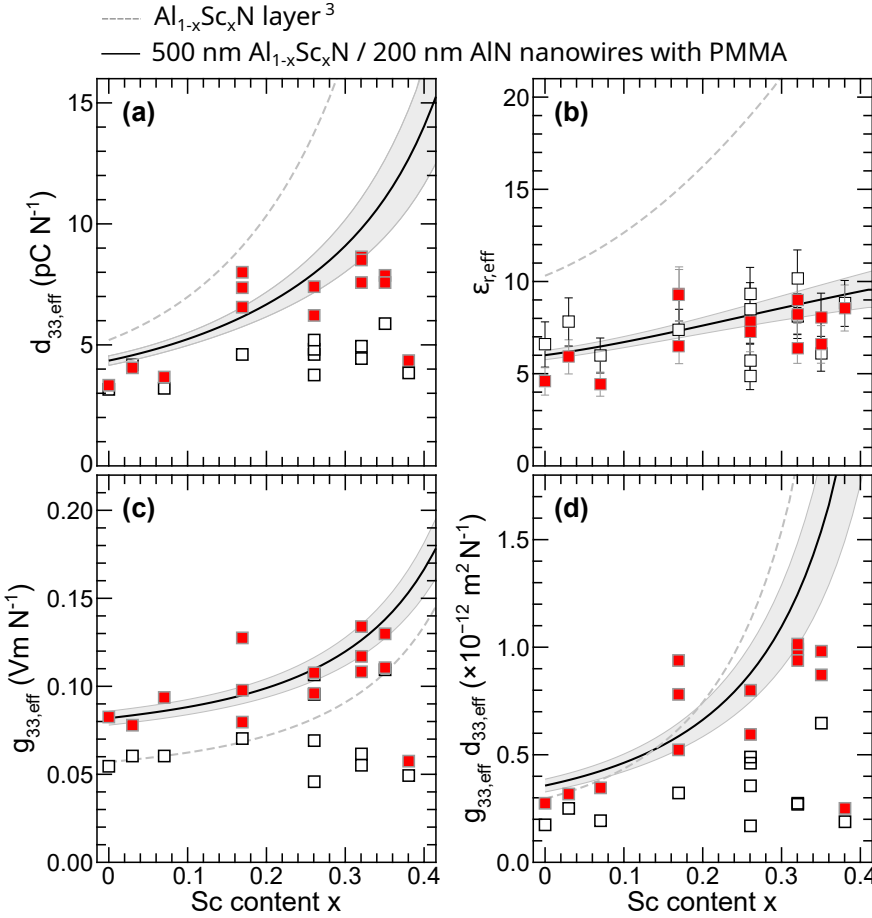


Figure 5: Comparison of experimental and theoretical effective piezoelectric and dielectric properties of the $\text{Al}_{1-x}\text{Sc}_x\text{N}$ VINGs. (a) Shows the piezoelectric charge coefficient, (b) the relative static permittivity, (c) piezoelectric voltage coefficient, and (d) energy-harvesting figure of merit as a function of Sc content x . Devices exhibiting the strongest experimental performance for each composition are highlighted in red. The gray dashed line in each panel denotes the corresponding trend reported for $\text{Al}_{1-x}\text{Sc}_x\text{N}$ thin films.³ The black solid line indicates the calculation of each effective parameter as a function of Sc content, while the shaded region represents the associated uncertainty.

tracted by simulating the impedance data with equivalent circuit models, as described in our previous work.¹⁶ Assuming a parallel plate capacitor geometry and taking into account the device dimensions, we then extract $\epsilon_{r,\text{eff}}$, which is shown for all devices in Figure 5b. Due to the effective-medium nature of the nanowire-polymer composite, $\epsilon_{r,\text{eff}}$ is strongly reduced compared to the dielectric permittivity of $\text{Al}_{1-x}\text{Sc}_x\text{N}$ layers (dashed, grey line). To explain this trend, we extend the model from Figure 5a to calculate $\epsilon_{r,\text{eff}}$ for the nanowire-polymer composites (see Section 4.2). Assuming the same device geometry, we find an excellent agreement with the experimental data.

The reduction of $\epsilon_{r,\text{eff}}$ with respect to $\text{Al}_{1-x}\text{Sc}_x\text{N}$ thin films is expected to enhance the sensing efficiency of our devices. Indeed, by combining the results from Figures 5a-b, the experimentally extracted $g_{33,\text{eff}}$ values of the best devices exceed those expected for $\text{Al}_{1-x}\text{Sc}_x\text{N}$ thin films, indicating that the reduction on $\epsilon_{r,\text{eff}}$ overcompensates the reduction of $d_{33,\text{eff}}$. This is confirmed by our model,

which predicts piezoelectric voltage coefficients approximately 1.5 times higher compared to the thin film case. Again, even higher $g_{33,\text{eff}}$ are anticipated for optimized device architectures combining an enhanced $d_{33,\text{eff}}$ with similar dielectric properties.

Finally, we evaluate the energy harvesting efficiency of our devices, defined as $g_{33,\text{eff}}d_{33,\text{eff}}$, and compare it to the expected performance of $\text{Al}_{1-x}\text{Sc}_x\text{N}$ thin films. As shown in Figure 5d, a comparable overall efficiency is achieved, despite slightly lower output at high Sc contents.

3 Conclusion

In conclusion, we have investigated the growth of $\text{Al}_{1-x}\text{Sc}_x\text{N}$ nanowires by plasma-assisted MBE. Phase separation into wurtzite AlN and rock-salt ScN occurs at growth temperatures above 700 °C, the $[0001]_{\text{AlN}}$ and $[001]_{\text{ScN}}$ directions being epitaxially aligned, consistent with previous studies.^{29,30} Lower

growth temperatures stabilize the desired wurtzite phase, where $\text{Al}_{1-x}\text{Sc}_x\text{N}$ nanowires are obtained in a wide compositional range ($0 \leq x < 0.35$). The highly insulating nature of our nanowires ensures a stable device operation when integrated into vertical nanogenerators. Furthermore, the increased incorporation of Sc boosts the effective piezoelectric charge coefficients of our devices up to 8.5 pCN^{-1} , clearly outperforming bulk AlN and approaching that of bulk ZnO. For Sc contents of $x > 0.35$, a drop in efficiency occurs due to an amorphization of the material, likely occurring before the phase transition towards the rock-salt $\text{Al}_{1-x}\text{Sc}_x\text{N}$ phase. Despite the lower charge output of our devices compared to $\text{Al}_{1-x}\text{Sc}_x\text{N}$ thin films, our nanogenerators exhibit a markedly improved voltage output and comparable energy harvesting efficiency. This behavior is attributed to a lower effective dielectric permittivity in the nanowire-polymer composite. Effective medium modeling further reveals that additional performance gains can be achieved by optimizing the device architecture. In particular, a strongly piezoelectric active region with low dielectric permittivity, sandwiched directly between two electrodes, promises maximum response. These results pave the way towards a new generation of devices that exploit the intrinsic advantages of nanowire architectures, enabling performance levels beyond what is feasible with $\text{Al}_{1-x}\text{Sc}_x\text{N}$ thin films.

4 Materials and Methods

4.1 Experimental details

$\text{Al}_{1-x}\text{Sc}_x\text{N}$ is grown by plasma-assisted MBE on around 200 nm long AlN nanowire stems, self-assembled on 400 nm-thick metallic TiN films, the latter described in our previous works.^{22,24} The AlN nanowires exhibit Al-polarity, as determined previously by several methods.^{16,22,35} To vary the composition of the growing $\text{Al}_{1-x}\text{Sc}_x\text{N}$ segments, we vary the Sc flux while keeping the Al and active N fluxes constant, as further detailed in Table 1. The Sc

flux was calibrated by determining the growth rate of ScN layers in the Sc-limited regime, while the active N flux was calibrated by determining the growth rate of GaN layers in the N-limited regime. All effusion cells are mounted with an angle of 38° with respect to the surface normal and growth is done under continuous sample rotation. The growth temperature of the wurtzite $\text{Al}_{1-x}\text{Sc}_x\text{N}$ nanowire ensembles is kept below 700°C and successively reduced as a function of Sc content in order to avoid phase separation and optimize for highest crystalline quality (cf. Table 1). Substrate temperatures above 500°C were measured via optical pyrometry at 920 nm, calibrated according to a procedure we established previously.^{22,24} For lower temperatures, a thermocouple positioned 10 mm behind the heater filament is used. Low-temperature calibration is based on the melting point of In, occurring at 156.6°C . Intermediate temperatures are estimated by a linear interpolation between pyrometric data and the In melting point. The crystallinity of the growing nanowires is monitored by RHEED, using an acceleration voltage of 20 kV.

Scanning electron microscopy is used to investigate the nanowire morphology using a Hitachi S4800. The structural properties of the nanowires are characterized using a laboratory x-ray diffraction system (Philips PANalytical X'Pert PRO MRD) equipped with a two-bounce hybrid monochromator Ge(220) for the $\text{Cu K}_{\alpha 1}$ source ($\lambda = 1.540598 \text{ \AA}$) and a 1 mm receiving slit in front of the x-ray detector. The microstructure of selected samples was studied by STEM, using a Titan SPECTRA 200 (ThermoFisher), equipped with a cold field emission gun and a Cs aberration probe corrector. A dual energy dispersive x-ray detector is used for EDX mapping. Cross-section specimens were prepared using standard mechanical grinding and dimpling methods, where final thinning was done using different acceleration voltages from 4 to 0.2 kV with Ar ions, in a Gatan precision ion polishing system.

The composition of all nanowire ensembles was determined using EDX spectroscopy (EDAX Octane Elect Super detector), excit-

Table 1: Growth conditions of $\text{Al}_{1-x}\text{Sc}_x\text{N}$ nanowires with different Sc content x .

Composition	Growth temperature (°C)	N flux ($\times 10^{15}$ at $\text{cm}^{-2}\text{s}^{-1}$)	Al flux ($\times 10^{14}$ at $\text{cm}^{-2}\text{s}^{-1}$)	Sc flux ($\times 10^{13}$ at $\text{cm}^{-2}\text{s}^{-1}$)
$\text{Al}_{0.03}\text{Sc}_{0.97}\text{N}$	660	1.5	2.2	1.1
$\text{Al}_{0.07}\text{Sc}_{0.93}\text{N}$	580	1.5	2.2	2.3
$\text{Al}_{0.17}\text{Sc}_{0.83}\text{N}$	500	1.5	2.2	4.3
$\text{Al}_{0.26}\text{Sc}_{0.74}\text{N}$	410	1.5	2.2	8.0
$\text{Al}_{0.32}\text{Sc}_{0.68}\text{N}$	410	1.5	2.2	10.5
$\text{Al}_{0.35}\text{Sc}_{0.65}\text{N}$	410	1.5	2.2	12.9
$\text{Al}_{0.38}\text{Sc}_{0.62}\text{N}$	240	1.5	2.2	16.7

ing the sample with an electron beam of an energy of 8 keV inside a scanning electron microscope (Zeizz Ultra 55). To extract the atomic concentrations of Al and Sc, we used the well-separated $\text{Al K}_{\alpha 1}$ and $\text{Sc K}_{\alpha 1}$ peaks and analyze them with the ZAF algorithm of the EDAX software,³⁷ thus including corrections for the detector efficiency, atomic number, absorption and fluorescence of x-rays. To exclude any impact of the AlN stems, the measurements were performed in the cross-section geometry.

Raman spectroscopy was performed at room temperature, with a 473 nm laser line used for excitation. The spectra were acquired on the sample cross-section in a back scattering geometry, employing an Olympus microscope objective with a magnification of 100 \times and a numerical aperture of 0.9. A custom-modified HR Evolution setup (Horiba) was used, with a 800 mm focal length monochromator equipped with a 1800 grooves cm^{-1} grating and a liquid nitrogen-cooled CCD detector. Spectral calibration was performed using the optical phonon of Si at 520.3 cm^{-1} as reference.

To test the piezoelectric response of our $\text{Al}_{1-x}\text{Sc}_x\text{N}$ nanowires, we process them into vertically integrated nanogenerators. To this end, a 2 % PMMA solution is spin-coated at 6000 rpm for 30 s onto the $\text{Al}_{1-x}\text{Sc}_x\text{N}$, forming a \approx 60 nm over-layer. After soft-baking at 180 °C for 5 min, this encapsulation provided mechanical stability and a uniform surface for the subsequent contact fabrication. We use electron beam evaporation to deposit circu-

lar top contacts with a diameter of 0.8–1 mm, consisting of 10 nm Ni and 100 nm Pt. Silver epoxy was then applied to the top contacts to improve the mechanical and electrical reliability. As bottom contact, we use the 400 nm-thick sputtered TiN substrate. The direct response of the nanogenerators is measured according to the Berlincourt principle³⁴ and applying a dynamic (0.3 to 150 Hz) sinusoidal force of 0.3–1 N, with a static preload of 2–7 N to ensure device stability. After measuring the piezoelectric signal, an impedance measurement was performed at the same position under the same static preload using an LCR meter (Keysight 4980AL) with an excitation voltage of 2 V and frequency ranging from 20 Hz to 1 MHz. The capacitance and resistance values of the devices under test were extracted using a parallel equivalent circuit model, as we have previously reported for GaN and AlN nanowires.¹⁶ Note that the $\varepsilon_{r,\text{eff}}$ shown in Figure 5b was extracted at 200 kHz to enable direct comparison with data available in the literature.³

4.2 Effective medium modeling

To evaluate the effective dielectric and piezoelectric properties of our $\text{Al}_{1-x}\text{Sc}_x\text{N}/\text{AlN}$ nanowire-polymer composites subjected to mechanical loading along the nanowire axis, we employed an effective medium modeling approach. This framework combines analytical homogenisation based on Reuss³⁸ and Voigt³⁹ averaging schemes, which correspond to iso-stress and iso-strain assumptions, re-

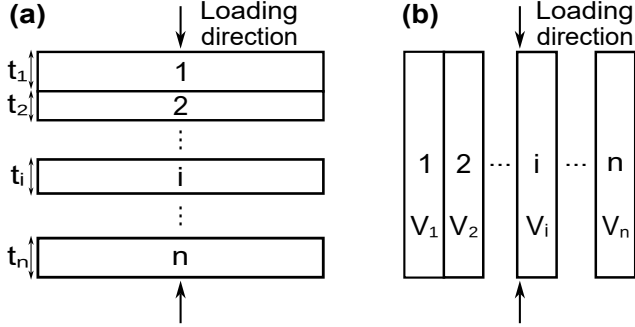


Figure 6: Schematic representation of a sequence of layers connected in series (a, Reuss) and in parallel (b, Voigt) with respect to the applied stress.

spectively. To derive expressions describing the effective medium, we begin with the fundamental constitutive equations of piezoelectricity for both the direct and inverse effects and apply the appropriate boundary conditions. In the experimental configuration of the Berlincourt method, the measurement is performed under a charge-compensation (short-circuit) regime; consequently, the electric field within the active piezoelectric medium can be assumed to be zero. The Reuss model assumes uniform stress throughout the layers, corresponding to a series (stacked) arrangement along the loading direction (Figure 6a). In contrast, the Voigt model assumes uniform strain across all layers, equivalent to a parallel configuration with respect to the applied load (Figure 6b).

Under the conditions described above, the effective properties of the heterostructure can be derived. The following expressions define the elastic compliance $S_{33,\text{eff}}$, the piezoelectric stress coefficient $e_{33,\text{eff}}$ and the dielectric constant $\varepsilon_{33,\text{eff}}$ of the effective medium.

Reuss Averaging:

$$\begin{aligned} S_{33,\text{eff}} &= \sum_i f_i S_{33,i} \\ \varepsilon_{r,\text{eff}} &= \left(\sum_i \frac{f_i}{\varepsilon_{r,i}} \right)^{-1} \\ e_{33,\text{eff}} &= \frac{\sum_i f_i S_{33,i} e_{33,i}}{\sum_i f_i S_{33,i}} \end{aligned} \quad (2)$$

Voigt Averaging:

$$\begin{aligned} S_{33,\text{eff}} &= \left(\sum_i \frac{f_i}{S_{33,i}} \right)^{-1} \\ \varepsilon_{r,\text{eff}} &= \sum_i f_i \varepsilon_{r,i} \\ e_{33,\text{eff}} &= \sum_i f_i e_{33,i} \end{aligned} \quad (3)$$

The f_i factors represent the fraction occupied by the i -th layer, which are determined by their thicknesses t_i in the Reuss case and volumes V_i in the Voigt case (cf. Figure 6). These two models provide simple methods for predicting the mechanical and electrical behavior of layered composites.

Acknowledgement The authors thank Doreen Steffen for TEM sample preparation, Nicole Volkmer for assistance in SEM measurements, Carsten Stemmler for his dedicated MBE maintenance and Bruno Fernandez for his support in sample processing. We are further grateful to Mingyun Yuan for critically reading the manuscript. This work was funded by Deutsche Forschungsgemeinschaft (490935200) and Agence Nationale de la Recherche (ANR-21-CE09-0044) through the project Nanoflex, and supported by COST Action OPERA from the European Network for Innovative and Advanced Epitaxy, CA20116 (www.cost.eu).

References

- (1) Jena, D.; Page, R.; Casamento, J.; Dang, P.; Singhal, J.; Zhang, Z.; Wright, J.; Khalsa, G.; Cho, Y.; Xing, H. G. The New Nitrides: Layered, Ferroelectric, Magnetic, Metallic and Superconducting Nitrides to Boost the GaN Photonics and Electronics Eco-System. *Jpn. J. Appl. Phys.* **2019**, *58*, SCo801, DOI: [10.7567/1347-4065/ab147b](https://doi.org/10.7567/1347-4065/ab147b).
- (2) Akiyama, M.; Kamohara, T.; Kano, K.; Teshigahara, A.; Takeuchi, Y.; Kawahara, N. Enhancement of Piezoelec-

tric Response in Scandium Aluminum Nitride Alloy Thin Films Prepared by Dual Reactive Cospattering. *Advanced Materials* **2009**, *21*, 593–596, DOI: [10.1002/adma.200802611](https://doi.org/10.1002/adma.200802611).

(3) Ambacher, O.; Christian, B.; Feil, N.; Urban, D. F.; Elsässer, C.; Prescher, M.; Kirste, L. Wurtzite ScAlN, InAlN, and GaAlN Crystals, a Comparison of Structural, Elastic, Dielectric, and Piezoelectric Properties. *J. Appl. Phys.* **2021**, *130*, 045102, DOI: [10.1063/5.0048647](https://doi.org/10.1063/5.0048647).

(4) Miyamoto, T.; Akiyama, T.; Kawamura, T. Theoretical Study on Structural Stability and Miscibility of ScAlN Alloys: Effect of Lattice Constraint. *Jpn. J. Appl. Phys.* **2025**, *64*, 01SP03, DOI: [10.35848/1347-4065/ad9bb9](https://doi.org/10.35848/1347-4065/ad9bb9).

(5) Fichtner, S.; Wolff, N.; Lofink, F.; Kienle, L.; Wagner, B. AlScN: A III-V Semiconductor Based Ferroelectric. *Journal of Applied Physics* **2019**, *125*, 114103, DOI: [10.1063/1.5084945](https://doi.org/10.1063/1.5084945).

(6) Urban, D. F.; Ambacher, O.; Elsässer, C. First-Principles Calculation of Electroacoustic Properties of Wurtzite (Al,Sc)N. *Phys. Rev. B* **2021**, *103*, 115204, DOI: [10.1103/PhysRevB.103.115204](https://doi.org/10.1103/PhysRevB.103.115204).

(7) Solonenko, D.; Lan, C.; Schmidt, C.; Stoeckel, C.; Hiller, K.; Zahn, D. R. T. Co-Sputtering of AlScN Thin Films on Pt(111): A Characterization by Raman and IR Spectroscopies. *J. Mater. Sci.* **2020**, *55*, 17061–17071, DOI: [10.1007/s10853-020-05244-8](https://doi.org/10.1007/s10853-020-05244-8).

(8) Solonenko, D.; Žukauskaitė, A.; Pilz, J.; Moridi, M.; Risquez, S. Raman Spectroscopy and Spectral Signatures of AlScN/Al₂O₃. *Micromachines* **2022**, *13*, 1961, DOI: [10.3390/mi13111961](https://doi.org/10.3390/mi13111961).

(9) Dinh, D. V.; Peiris, F.; Lähnemann, J.; Brandt, O. Optical Properties of ScN Layers Grown on Al₂O₃(0001) by

Plasma-Assisted Molecular Beam Epitaxy. *Appl. Phys. Lett.* **2023**, *123*, DOI: [10.1063/5.0164058](https://doi.org/10.1063/5.0164058).

(10) Grümbel, J.; Goldhahn, R.; Feneberg, M.; Oshima, Y.; Dubroka, A.; Ramsteiner, M. Band Gaps and Phonons of Quasi-Bulk Rocksalt ScN. *Phys. Rev. Materials* **2024**, *8*, DOI: [10.1103/physrevmaterials.8.1071601](https://doi.org/10.1103/physrevmaterials.8.1071601).

(11) Niewa, R.; Zherebtsov, D. A.; Kirchner, M.; Schmidt, M.; Schnelle, W. New Ways to High-Quality Bulk Scandium Nitride. *Chem. Mater.* **2004**, *16*, 5445–5451, DOI: [10.1021/cm048667y](https://doi.org/10.1021/cm048667y).

(12) Nilsson, D.; Janzén, E.; Kakanakova-Georgieva, A. Lattice Parameters of AlN Bulk, Homoepitaxial and Heteroepitaxial Material. *J. Phys. D: Appl. Phys.* **2016**, *49*, 175108, DOI: [10.1088/0022-3727/49/17/175108](https://doi.org/10.1088/0022-3727/49/17/175108).

(13) Wang, Z. L.; Song, J. Piezoelectric Nanogenerators Based on Zinc Oxide Nanowire Arrays. *Science* **2006**, *312*, 242–246, DOI: [10.1126/science.1124005](https://doi.org/10.1126/science.1124005).

(14) Zhang, X.; Dubrovskii, V. G.; Sibirev, N. V.; Ren, X. Analytical Study of Elastic Relaxation and Plastic Deformation in Nanostructures on Lattice Mismatched Substrates. *Cryst. Growth Des.* **2011**, *11*, 5441–5448, DOI: [10.1021/cg201029x](https://doi.org/10.1021/cg201029x).

(15) Ellmer, K.; Bikowski, A. Intrinsic and Extrinsic Doping of ZnO and ZnO Alloys. *J. Phys. D: Appl. Phys.* **2016**, *49*, 413002, DOI: [10.1088/0022-3727/49/41/413002](https://doi.org/10.1088/0022-3727/49/41/413002).

(16) Buatip, N.; Auzelle, T.; John, P.; Rauwerdink, S.; Sodhi, M.; Salaün, M.; Fernandez, B.; Monroy, E.; Mornex, D.; Bowen, C. R.; Songmuang, R. AlN Nanowire-Based Vertically Integrated Piezoelectric Nanogenerators. *ACS Appl. Nano Mater.* **2024**, *7*, 15798–15807.

(17) Ambacher, O.; Majewski, J.; Miskys, C.; Link, A.; Hermann, M.; Eickhoff, M.;

Stutzmann, M.; Bernardini, F.; Fiorenini, V.; Tilak, V.; Schaff, B.; Eastman, L. F. Pyroelectric Properties of Al(In)GaN/GaN Hetero- and Quantum Well Structures. *J. Phys.: Condens. Matter* **2002**, *14*, 3399–3434, DOI: [10.1088/0953-8984/14/13/302](https://doi.org/10.1088/0953-8984/14/13/302).

(18) Lu, Y.; Emanetoglu, N. W.; Chen, Y. *Zinc Oxide Bulk, Thin Films and Nanostructures*; Elsevier, 2006; pp 443–489, DOI: [10.1016/B978-008044722-3/50013-0](https://doi.org/10.1016/B978-008044722-3/50013-0).

(19) Bohnen, T.; Van Dreumel, G. W. G.; Hageman, P. R.; Algra, R. E.; Van Enckevort, W. J. P.; Vlieg, E.; Verheijen, M. A.; Edgar, J. H. Growth of Scandium Aluminum Nitride Nanowires on ScN(111) Films on 6H-SiC Substrates by HVPE. *Physica Status Solidi (a)* **2009**, *206*, 2809–2815, DOI: [10.1002/pssa.200925060](https://doi.org/10.1002/pssa.200925060).

(20) Zhang, X.; Xu, W.; Meng, W. J.; Meng, A. C. Single Crystal Ferroelectric AlScN Nanowires. *CrystEngComm* **2024**, *26*, 180–191, DOI: [10.1039/D3CE00990D](https://doi.org/10.1039/D3CE00990D).

(21) Wang, D.; Wang, P.; Mondal, S.; Hu, M.; Wu, Y.; Wang, D.; Sun, K.; Mi, Z. Nanoscale Engineering of Wurtzite Ferroelectrics: Unveiling Phase Transition and Ferroelectric Switching in ScAlN Nanowires. *ACS Appl. Nano Mater.* **2024**, *7*, 26756–26764, DOI: [10.1021/acsanm.4c04549](https://doi.org/10.1021/acsanm.4c04549).

(22) Azadmand, M.; Auzelle, T.; Lähnemann, J.; Gao, G.; Nicolai, L.; Ramsteiner, M.; Trampert, A.; Sanginetti, S.; Brandt, O.; Geelhaar, L. Self-Assembly of Well-Separated AlN Nanowires Directly on Sputtered Metallic TiN Films. *Phys. Status Solidi - Rapid Res. Lett.* **2020**, *14*, 1900615, DOI: [10.1002/pssr.201900615](https://doi.org/10.1002/pssr.201900615).

(23) Auzelle, T.; Oliva, M.; John, P.; Ramsteiner, M.; Trampert, A.; Geelhaar, L.; Brandt, O. Density Control of GaN Nanowires at the Wafer Scale Using Self-Assembled SiN_x Patches on Sputtered TiN(111). *Nanotechnology* **2023**, *34*, 375602, DOI: [10.1088/1361-6528/acdde8](https://doi.org/10.1088/1361-6528/acdde8).

(24) John, P.; Gómez Ruiz, M.; Van Deurzen, L.; Lähnemann, J.; Trampert, A.; Geelhaar, L.; Brandt, O.; Auzelle, T. Growth Kinetics and Substrate Stability during High-Temperature Molecular Beam Epitaxy of AlN Nanowires. *Nanotechnology* **2023**, *34*, 465605, DOI: [10.1088/1361-6528/acefd8](https://doi.org/10.1088/1361-6528/acefd8).

(25) Cheng, C.; Fan, H. J. Branched Nanowires: Synthesis and Energy Applications. *Nano Today* **2012**, *7*, 327–343, DOI: [10.1016/j.nantod.2012.06.002](https://doi.org/10.1016/j.nantod.2012.06.002).

(26) Lao, J. Y.; Wen, J. G.; Ren, Z. F. Hierarchical ZnO Nanostructures. *Nano Lett.* **2002**, *2*, 1287–1291, DOI: [10.1021/nl025753t](https://doi.org/10.1021/nl025753t).

(27) Daudin, B.; Siladie, A.-M.; Gruart, M.; Den Hertog, M.; Bougerol, C.; Haas, B.; Rouvière, J.-L.; Robin, E.; Recio-Carretero, M.-J.; Garro, N.; Cros, A. The Role of Surface Diffusion in the Growth Mechanism of III-nitride Nanowires and Nanotubes. *Nanotechnology* **2021**, *32*, 085606, DOI: [10.1088/1361-6528/abc780](https://doi.org/10.1088/1361-6528/abc780).

(28) Satoh, S.; Ohtaka, K.; Shimatsu, T.; Tanaka, S. Crystal Structure Deformation and Phase Transition of AlScN Thin Films in Whole Sc Concentration Range. *J. Appl. Phys.* **2022**, *132*, DOI: [10.1063/5.0087505](https://doi.org/10.1063/5.0087505).

(29) John, P.; Trampert, A.; Van Dinh, D.; Spallek, D.; Lähnemann, J.; Kaganer, V. M.; Geelhaar, L.; Brandt, O.; Auzelle, T. ScN/GaN(1100): A New Platform for the Epitaxy of Twin-Free Metal–Semiconductor Heterostructures. *Nano Lett.* **2024**, *24*, 6233–6239, DOI: [10.1021/acs.nanolett.4c00659](https://doi.org/10.1021/acs.nanolett.4c00659).

(30) Höglund, C.; Alling, B.; Birch, J.; Beckers, M.; Persson, P. O. Å.; Bae-

htz, C.; Czigány, Z.; Jensen, J.; Hultman, L. Effects of Volume Mismatch and Electronic Structure on the Decomposition of ScAlN and TiAlN Solid Solutions. *Phys. Rev. B* **2010**, *81*, DOI: [10.1103/physrevb.81.224101](https://doi.org/10.1103/physrevb.81.224101).

(31) Wölz, M.; Hauswald, C.; Flissikowski, T.; Gotschke, T.; Fernández-Garrido, S.; Brandt, O.; Grahn, H. T.; Geelhaar, L.; Riechert, H. Epitaxial Growth of GaN Nanowires with High Structural Perfection on a Metallic TiN Film. *Nano Lett.* **2015**, *15*, 3743–3747, DOI: [10.1021/acs.nanolett.5b00251](https://doi.org/10.1021/acs.nanolett.5b00251).

(32) Zhang, X.; Stach, E. A.; Meng, W. J.; Meng, A. C. Nanoscale Compositional Segregation in Epitaxial AlScN on Si (111). *Nanoscale Horiz.* **2023**, *8*, 674–684, DOI: [10.1039/D2NH00567K](https://doi.org/10.1039/D2NH00567K).

(33) Eaglesham, D. J. Semiconductor Molecular-Beam Epitaxy at Low Temperatures. *J. Appl. Phys.* **1995**, *77*, 3597–3617, DOI: [10.1063/1.358597](https://doi.org/10.1063/1.358597).

(34) Stewart, M.; Battrick, W.; Cain, M. G. *Measuring Piezoelectric D₃₃ Coefficients Using the Direct Method. Measurement Good Practice Guide*; National Physical Laboratory, Teddington, UK, 2021, ISSN: 1368-6550.

(35) Jaloustre, L.; Le Denmat, S.; Auzelle, T.; Azadmand, M.; Geelhaar, L.; Dahlem, F.; Songmuang, R. Toward Quantitative Measurements of Piezoelectricity in III-N Semiconductor Nanowires. *ACS Appl. Nano Mater.* **2021**, *4*, 43–52, DOI: [10.1021/acsanm.0c02078](https://doi.org/10.1021/acsanm.0c02078).

(36) Kang, J.; Jose, R.-M.; Oliva, M.; Auzelle, T.; Ruiz, M. G.; Tahraoui, A.; Lähnemann, J.; Brandt, O.; Geelhaar, L. Uniform Large-Area Surface Patterning Achieved by Metal Dewetting for the Top-down Fabrication of GaN Nanowire Ensembles. *Nanotechnology* **2024**, *35*, 375301, DOI: [10.1088/1361-6528/ad5682](https://doi.org/10.1088/1361-6528/ad5682).

(37) Eggert, F. Abilities Towards Improved Accuracy in EPMA. *Microsc Microanal* **2021**, *27*, 1108–1110, DOI: [10.1017/S1431927621004165](https://doi.org/10.1017/S1431927621004165).

(38) Reuss, A. Berechnung Der Fließgrenze von Mischkristallen Auf Grund Der Plastizitätsbedingung Für Einkristalle . *Z Angew Math Mech* **1929**, *9*, 49–58, DOI: [10.1002/zamm.19290090104](https://doi.org/10.1002/zamm.19290090104).

(39) Voigt, W. Ueber Die Beziehung Zwischen Den Beiden Elasticitätsconstanten Isotroper Körper. *Annalen der Physik* **1889**, *274*, 573–587, DOI: [10.1002/andp.18892741206](https://doi.org/10.1002/andp.18892741206).